International Journal of Minerals, Metallurgy and Materials
Volume 27, Number 2, February 2020, Page 200
https://doi.org/10.1007/s12613-019-1875-9

Simulation of macrosegregation in a 36-t steel ingot using a multiphase model

Zhuo Chen and Hou-fa Shen

Key Laboratory for Advanced Material Processing Technology, Ministry of Education, School of Material Science and Engineering, Tsinghua University, Beijing 100083, China

(Received: 14 February 2019; revised: 13 May 2019; accepted: 14 May 2019)

Abstract: Macrosegregation is the major defect in large steel ingots caused by solute partitioning and melt convection during casting. In this study, a three-phase (liquid, columnar dendrites, and equiaxed grains) model is proposed to simulate macrosegregation in a 36-t steel ingot. A supplementary set of conservation equations are employed in the model such that two types of equiaxed grains, either settling or adhering to the solid shell, are well simulated. The predicted concentration agrees quantitatively with the experimental value. A negative segregation cone was located at the bottom owing to the grain settlement and solute-enriched melt leaving from the mushy zone. The interdendritic liquid flow was carefully analyzed, and the formation of A-type segregations in the mid-height of the ingot is discussed. Negative segregation was observed near the riser neck due to the specific relationship between flow direction and temperature gradient. Additionally, the as-cast macrostructure of the ingot is presented, including the grain size distribution and columnar–equiaxed transition.

Keywords: macrosegregation; multiphase model; transportation; solidification; steel ingot

Nomenclature

List of symbols

g Volume fraction;
$\boldsymbol{u}$ Velocity, $m \cdot s^{-1}$;
ρ Density, $kg \cdot m^{-3}$;
Γ Phase transfer rate, $kg \cdot m^{-3} \cdot s^{-1}$;
μ Viscosity, $kg \cdot m^{-1} \cdot s^{-1}$;
p Pressure, Pa;
K Drag coefficient, $kg \cdot m^{-3} \cdot s^{-1}$;
C Species content, wt%;
R Grain radius, m;
k Thermal conductivity, $W \cdot m^{-1} \cdot k^{-1}$;
h Enthalpy, $J \cdot kg^{-1}$;
$\dot{N}$ Nucleation rate, $m^{-3} \cdot s^{-1}$;
n Number density of equiaxed grains, m^{-3};
n_{max} Maximum grain number density, m^{-3};
ΔT_N Undercooling for maximum nucleation rate, K;
ΔT_σ Gaussian distribution width of nucleation, K;
δ Factor of diffusion length;
β_T Thermal expansion coefficient, K^{-1};
β_C Concentration expansion coefficient;
β_{sl} Density difference between liquid and solid.

Subscripts and superscripts

l Liquid phase;
c Columnar dendrite;
e Free-floating equiaxed grain;
es Stationary equiaxed grain;
ref Reference value;
* Equilibrium value at the interface;
b Buoyancy term.

1. Introduction

Chemical inhomogeneity on a large scale, also known as macrosegregation, is a defect widely found in steel products. Macrosegregation results from solute partitioning, thermosolutal convection, and equiaxed settlement during solidification. A typical macrosegregation in an ingot contains a positive segregated zone at the top and a negative segregated zone at the bottom. Moreover, A-type segregations are always found in the middle of the ingot.

Since the 1960s, many investigations have been performed to predict the segregation pattern of large ingots for

Corresponding author: Hou-fa Shen E-mail: shen@tsinghua.edu.cn

the interest of industrial manufacturing [1–2]. Prakash [3], Ni and Beckermann [4] firstly developed an advanced numerical modeling technique, known as a two-phase model. This technique, based on the volume-averaging method, assumed a fixed solid phase to analyze the motion of the interdendritic liquid. A. Ludwig and M. Wu developed a three-phase approach to simulate the solidification of steel ingot [5]. The model contained liquid, columnar dendrites, and equiaxed grains. The columnar phase was assumed to adhere to the wall, while the equiaxed phase moved during solidification. By this approach, the negative segregation cone at the bottom of the ingot, induced by grain settlement, was well predicted. Combeau *et al.* [6] performed an in-depth research of grain settlement with a two-phase model. They studied the motion of equiaxed grains and its influence factors, such as grain morphology. The trend of grain settlement was found to significantly affect the macrosegregation features. Wu *et al.* [7–8] proposed a five-phase mixed columnar–equiaxed model. In this model, the interdendritic melt of both columnar dendrite and equiaxed grains were treated as independent phase, such that the interaction between dendrite and interdendritic melt could be explicitly modeled. A four-phase model in which air was involved in the multiphase frame was established by Wu *et al.* [9]. The four-phase model accounted for shrinkage during solidification and effectively predicted the positive segregation in the top of the ingot.

Duan *et al.* [10] cast and chemically analyzed a 36-t steel ingot, and sufficient macrosegregation data were provided. According to the experimental result, typical macrosegregation features such as negative segregation at the bottom and positive segregation at the top were noticed. Moreover, the negative segregation along the side wall of the hot top was found. Tu *et al.* [11] developed a multicomponent three-phase model to predict the macrosegregation of a 36-t steel ingot. Their simulation results showed that the major segregation features, together with the shrinkage cavity, were well reproduced and a high-leveled general agreement was obtained. Wu *et al.* [12], using a four-phase model, also carried out a simulation of such an ingot. In addition to the macrosegregation and shrinkage cavity, the porosity was predicted using this model.

However, its formation mechanism is still unclear due to the complex macrosegregation in large steel ingots. Taking the 36-t steel ingots as an example, the evolution of bottom-located negative segregation and mid-located channel segregation still requires clearer descriptions. The negative segregation near the riser neck also requires further study. Moreover, the solidification structure should be emphasized, because the as-cast macrostructure of steel ingots is closely related to macrosegregation.

In this study, a multiphase model is proposed to simulate macrosegregation in the 36-t steel ingot. This model includes liquid, columnar dendrites, and equiaxed grains. The motion of equiaxed grains, whether free-floating or adhering to the solid shell, is simulated by this model using a set of supplementary conservation equations. With this model, a detailed study regarding the formation of bottom-located negative segregation, channel segregation, and top-located positive segregation is performed. The formation of negative segregation near the riser neck is also investigated and explained using a mathematical criterion. An as-cast macrostructure simulation, including the grain size distribution and columnar–equiaxed transition (CET), is performed. The simulation result indicates good quantitative agreement with the experimental measurement.

2. Model description

The model consists of three phases: liquid, columnar dendrite, and equiaxed grains. The conservation equations of mass, momentum, species, and energy for each phase are solved simultaneously under a volume-averaged frame. In addition, a new set of conservation equations are supplemented into the model, and this facilitates the simulation of the nucleation and growth of motionless equiaxed grains that adhere to the solid shell (marked with subscript es). The model equations and discussion are listed below.

Conservation equations in four-phase model:

Mass conservation:

$$\frac{\partial}{\partial t}(g_{\mathrm{l}}\rho_{\mathrm{l}}) + \nabla\cdot(g_{\mathrm{l}}\rho_{\mathrm{l}}\boldsymbol{u}_{\mathrm{l}}) = -\Gamma_{\mathrm{cl}} - \Gamma_{\mathrm{el}} - \Gamma_{\mathrm{esl}} \tag{1}$$

$$\frac{\partial}{\partial t}(g_{\mathrm{c}}\rho_{\mathrm{c}}) = \Gamma_{\mathrm{cl}} \tag{2}$$

$$\frac{\partial}{\partial t}(g_{\mathrm{e}}\rho_{\mathrm{e}}) + \nabla\cdot(g_{\mathrm{e}}\rho_{\mathrm{e}}\boldsymbol{u}_{\mathrm{e}}) = -\Gamma_{\mathrm{el}} \tag{3}$$

$$\frac{\partial}{\partial t}(g_{\mathrm{es}}\rho_{\mathrm{es}}) = \Gamma_{\mathrm{esl}} \tag{4}$$

Momentum conservation:

$$\begin{aligned}\frac{\partial}{\partial t}(g_{\mathrm{l}}\rho_{\mathrm{l}}\boldsymbol{u}_{\mathrm{l}}) + \nabla\cdot(g_{\mathrm{l}}\rho_{\mathrm{l}}\boldsymbol{u}_{\mathrm{l}}\cdot\boldsymbol{u}_{\mathrm{l}}) = \\ -g_{\mathrm{l}}\nabla p + \nabla\cdot(\mu_{\mathrm{l}}g_{\mathrm{l}}\nabla\boldsymbol{u}_{\mathrm{l}}) + g_{\mathrm{l}}\rho_{\mathrm{l}}^{\mathrm{b}}\boldsymbol{g} + K_{\mathrm{cl}}(\boldsymbol{u}_{\mathrm{c}} - \boldsymbol{u}_{\mathrm{l}}) + \\ K_{\mathrm{el}}(\boldsymbol{u}_{\mathrm{e}} - \boldsymbol{u}_{\mathrm{l}}) + K_{\mathrm{esl}}(\boldsymbol{u}_{\mathrm{es}} - \boldsymbol{u}_{\mathrm{l}})\end{aligned} \tag{5}$$

$$\begin{aligned}\frac{\partial}{\partial t}(g_{\mathrm{e}}\rho_{\mathrm{e}}\boldsymbol{u}_{\mathrm{e}}) + \nabla\cdot(g_{\mathrm{e}}\rho_{\mathrm{e}}\boldsymbol{u}_{\mathrm{e}}\cdot\boldsymbol{u}_{\mathrm{e}}) = \\ -g_{\mathrm{e}}\nabla p + \nabla\cdot(\mu_{\mathrm{e}}g_{\mathrm{e}}\nabla\boldsymbol{u}_{\mathrm{e}}) + g_{\mathrm{e}}\rho_{\mathrm{s}}^{\mathrm{b}}\boldsymbol{g} + K_{\mathrm{le}}(\boldsymbol{u}_{\mathrm{l}} - \boldsymbol{u}_{\mathrm{e}}) + \\ K_{\mathrm{ce}}(\boldsymbol{u}_{\mathrm{c}} - \boldsymbol{u}_{\mathrm{e}}) + K_{\mathrm{ese}}(\boldsymbol{u}_{\mathrm{es}} - \boldsymbol{u}_{\mathrm{e}})\end{aligned} \tag{6}$$

Species conservation:

$$\frac{\partial}{\partial t}(g_l\rho_l C_l)+\nabla\cdot(g_l\rho_l C_l\boldsymbol{u}_l)= \nabla\cdot(g_l\rho_l D_l\nabla C_l)-C_c^*\Gamma_{cl}-C_e^*\Gamma_{el}-C_{es}^*\Gamma_{esl} \quad (7)$$

$$\frac{\partial}{\partial t}(g_c\rho_c C_c)=\nabla\cdot(g_c\rho_c D_c\nabla C_c)+C_c^*\Gamma_{cl} \quad (8)$$

$$\frac{\partial}{\partial t}(g_e\rho_e C_e)+\nabla\cdot(g_e\rho_e C_e\boldsymbol{u}_e)=\nabla\cdot(g_e\rho_e D_e\nabla C_e)+C_e^*\Gamma_{el} \quad (9)$$

$$\frac{\partial}{\partial t}(g_{es}\rho_{es} C_{es})=\nabla\cdot(g_{es}\rho_{es} D_{es}\nabla C_{es})+C_{es}^*\Gamma_{esl} \quad (10)$$

Energy conservation:

$$\frac{\partial}{\partial t}(g_l\rho_l h_l)+\nabla\cdot(g_l\rho_l h_l\boldsymbol{u}_l)= \nabla\cdot(g_l\rho_l k_l\nabla T_l)-Q_l^*\Gamma_{cl}-Q_l^*\Gamma_{el}-Q_l^*\Gamma_{esl} \quad (11)$$

$$\frac{\partial}{\partial t}(g_c\rho_c h_c)=\nabla\cdot(g_c\rho_c k_c\nabla T_c)+Q_l^*\Gamma_{cl} \quad (12)$$

$$\frac{\partial}{\partial t}(g_e\rho_e h_e)+\nabla\cdot(g_e\rho_e h_e\boldsymbol{u}_e)=\nabla\cdot(g_e\rho_e k_e\nabla T_e)+Q_l^*\Gamma_{el} \quad (13)$$

$$\frac{\partial}{\partial t}(g_{es}\rho_{es} h_{es})=\nabla\cdot(g_{es}\rho_{es} k_{es}\nabla T_{es})+Q_l^*\Gamma_{esl} \quad (14)$$

Kinetics of grain growth and motion:

Number density:

$$\frac{\partial}{\partial t}n+\nabla(\boldsymbol{u}_e n)=\dot{N} \quad (15)$$

Nucleation model:

$$\dot{N}=\frac{\mathrm{d}\Delta T}{\mathrm{d}t}\frac{n_{max}}{\sqrt{2\pi}\Delta T_\sigma}\exp\left[-\frac{1}{2}\left(\frac{\Delta T-\Delta T_N}{\Delta T_\sigma}\right)^2\right] \quad (16)$$

Density:

$$\rho_l^b=\rho_{ref}(1-\beta_T(T_l-T_{ref})-\beta_C(C_l-C_{ref})) \quad (17)$$

$$\rho_s^b=\rho_{ref}[1+\beta_{sl}-\beta_T(T_s-T_{ref})-\beta_C(C_s-C_{ref})] \quad (18)$$

Drag coefficient for each couple of phases:

$$K_{pq}=M_{pq}\cdot g_q \quad (19)$$

Viscosity for equiaxed grain:

$$\mu_s=\frac{\mu_l}{g_s}\left[\left(1-\frac{g_s}{g_l}\right)^{-2.5g_{sc}}-(1-g_s)\right] \quad (20)$$

Grain-growth rate:

$$v_R=\frac{D_l}{R_s}\left(\frac{C_l^*-C_l}{C_l^*-C_s^*}\right)\times\delta \quad (21)$$

(1) As defined by this model, the equiaxed grains belong to one phase but exhibit different motion states. Apart from the free-floating equiaxed grains, those grains that nucleate and grow while adhering to the solid shell should be simulated with independent conservation equations. During solidification, the nucleation rates of both types of equiaxed grains are adjusted according to a criterion that is derived from the previous research [13–14]. The schematic of two types of equiaxed grains and their relationship with the flow intensity are illustrated in Fig. 1. Schematically, the different sizes of arrows and lines are used to denote the different flow intensity of liquid. In Fig. 1(a), owing to the intensive liquid flow, the nuclei of equiaxed grains are taken away from the solid shell and settle. In Fig. 1(b), the nuclei grow motionlessly by the shell because the melt convection is weak. The criterion is related to the liquid velocity and the solid volume fraction, and its influence on the final concentration distribution is discussed in this work.

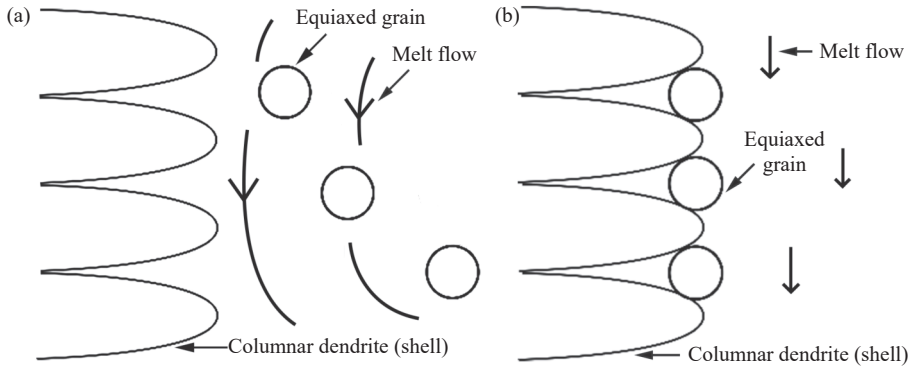

Fig. 1. Schematic of moving equiaxed grains (a) and stationary equiaxed grains (b).

(2) The momentum equation of columnar dendrite is not listed because the phase does not move during formation. Technically, a large negative value is added to the source term such that the velocity is reduced to zero. Similarly, the supplementary equations of motionless equiaxed grains do not include the momentum function.

(3) The material is simplified as a binary alloy, and the only species considered is carbon. A linearized Fe-C phase diagram is employed, whereby the partition coefficient (k) and liquidus slope (m) are constant.

(4) The equiaxed grains are considered as a mobile phase with a dynamic viscosity, defined by Eq. (20). Details of the

equation can be found in the paper by Ludwig and Wu [15].

(5) The grain-growth kinetics for columnar dendrite and equiaxed grain are governed by species diffusion. In Eq. (21), the difference term accounts for the species flux across the interface, and δ denotes the factor of diffusion length.

(6) The drag force coefficients between each phase couple are defined by Eq. (19). The subscript p denotes the primary phase and q denotes the secondary phase. For example, when considering the drag between the melt and equiaxed grains, p represents the liquid and q represents the equiaxed grains. M_{pq} is a large empirical value that can be set to 10^8.

(7) During solidification, the columnar dendrite originates from the chilled wall and proceeds toward the bulk liquid, and its tip front is tracked by a method similar to that of Wu *et al*. [5]. The free-floating equiaxed grains nucleate anywhere provided that the undercooling is achieved. Furthermore, remelting is considered in this model.

(8) This model accounts for the macrostructure, including the distribution of grain size and CET. Once the calculation volume of a cell is packed by the equiaxed grains at a critical fraction, the growth of columnar dendrite is stopped. The critical value is set to 0.49 [16].

(9) The boundary conditions for this simulation are derived from those reported by Duan *et al*. [10].

(10) Solidification shrinkage is not considered in this model.

3. Experiment and calculation parameters

This model was applied to a 36-t steel ingot. This ingot was cast and chemically analyzed at China International Trust and Investment Corporation (CITIC) Heavy Industries Co., Ltd. The shape and dimensions of the ingot are illustrated in Fig. 2. The cylindrical ingot was 3200 mm in height and 1200 mm in mean diameter. The ingot was filled from the bottom with molten steel at 1500°C. The carbon content of the liquid was 0.51wt%. The top of the ingot was covered by an exothermic powder and refractory materials at the outer surface.

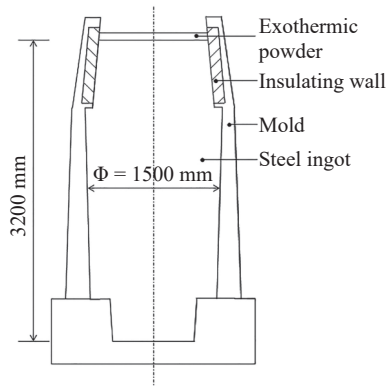

Fig. 2. Configuration of the 36-t steel ingot.

As reported by Duan *et al*. [10], the major macrosegregation features include bottom-located negative segregation and top-located positive segregation. The channel segregation was found in the mid-height of the ingot, and the negative segregation was found close to the riser neck.

For simplicity, a two-dimensional axisymmetric mesh was applied to simulate the macrosegregation on the vertical section of this ingot. The momentum equations were solved using the semi-implicit method for pressure-linked equations consistent algorithm. Table 1 lists the thermodynamic properties and parameters necessary for the simulation. The calculation domain was composed of more than 8000 cells with a size of 10 mm × 10 mm. The time step was initially set to 0.01 s and gradually increased to 0.1 s as the calculation proceeded stably.

Table 1. Parameters used in the simulation of steel ingot

Density, ρ / (kg·m^{-3})	Solid-liquid density difference, $\Delta\rho$ / (kg·m^{-3})	Melting temperature of pure iron, T_m / K	Liquidus slope, m_l / (K·wt%$^{-1}$)	Partition coefficient, k_p
6990	150	1805	−80.45	0.314
Latent heat, L / (J·kg^{-1})	Specific heat, c/ (J·kg^{-1}·K^{-1})	Thermal conductivity, k / (W·m^{-1}K^{-1})	Liquid viscosity, μ_l / (kg·m^{-1}·s^{-1})	Liquid solute diffusion coefficient, D_l / (m^2·s^{-1})
2.71×10^5	500	34	4.2×10^{-3}	2×10^{-8}
Solid solute diffusion coefficient, D_s / (m^2·s^{-1})	Pouring temperature, T_i /K	Thermal expansion coefficient, β_T / K^{-1}	Concentration expansion coefficient, β_C	Maximum equiaxed grain number density, n_{max} /m^{-3}
1×10^{-9}	1770	1.07×10^{-4}	1.4	1×10^{10}
Critical volume fraction, g_{sc}	Undercooling for maximum nucleation rate, ΔT_N / K	Gaussian distribution width of nucleation, ΔT_σ / K	Factor of diffusion length, δ	
0.6	5	2	10	

4. Results and discussion

4.1. Macrosegregation and comparison

The solidification sequence is shown in Fig. 3. In each of the four subfigures, the contours on the left show the progression of the solid shell, and those on the right show the evolution of macrosegregation.

At 1000 s (Fig. 3(a)), the liquid close to the chilled wall was lower in temperature and higher in density. The density difference caused the liquid to flow down with a maximum velocity of 40 mm/s. The flow diverted to an upward direction at the bottom of the ingot, and therefore, a clockwise circulation was formed in the bulk domain. The solidification at this stage was rapid because of the chilling mold, and the precise simulation of this phenomenon is significant to the prediction of the macrostructure and macrosegregation. The growth of columnar dendrite dominated in this solidification period because of the large-temperature gradient, and few equiaxed grains were found in the solid shell. Meanwhile, the solute-enriched interdendritic melt could hardly escape from the mushy zone and the shell exhibited a concentration identical to the initial value.

As solidification proceeded, the growth of columnar dendrite decelerated owing to the lower temperature gradient, and the formation of free-floating equiaxed grain started to become dominant. At 6000 s (Fig. 3(b)), a broad mushy zone consisting of equiaxed grains and liquid was found at the bottom of the ingot. A conic negative segregation was observed in the lower part as well. For the flow close to the shell, it has been reported that the solutal buoyancy should exceed the thermal buoyancy on the driving force [13]. The balance of these two opposite forces results in an upward direction of the flow. However, in this study, the flow direction was not reversed during the process, and the circumfluence remained clockwise. This is owing to the settlement of equiaxed grains, whose drag force imposed on the liquid retained the downward flow near the shell. The effect of the settling grains is further discussed later.

At 15000 s (Fig. 3(c)), the solid shell was thick but not flat. Streak-like A-type segregations were found beneath the shell surface. A cone of negative segregation, as a typical macrosegregation feature, was formed in the lower part of the ingot. The velocity of liquid flow was lower than that in Fig. 3(a) by an order of magnitude. At this stage, as defined by the model, more equiaxed grains will nucleate and grow while adhering to the solid shell without settling. In addition, a negative segregation was observed close to the riser neck. This negative segregation will be discussed later.

At the final stage of solidification, the remaining liquid began to solidify, and a positive segregation was formed at the top of the ingot (Fig. 3(d)). Because of the uniform temperature and high solute concentration in the liquid, such solidification requires a long time and motionless equiaxed grains sufficiently develop. Consequently, the hot top contained equiaxed grains at a higher volume fraction than other regions.

Fig. 4 shows the final segregation map and solidification structure. As illustrated in Fig. 4(a), the negative segregation cone was approximately one-third the ingot height, and the positive segregation occupied half the height. Streak-like A-type segregations were located at the middle of the ingot, with an inclined angle of approximately 60°. Thus, the simulation reproduced the experimental result.

A macrostructure map was obtained through the simulation. Fig. 4(b) shows the volume fraction of the equiaxed

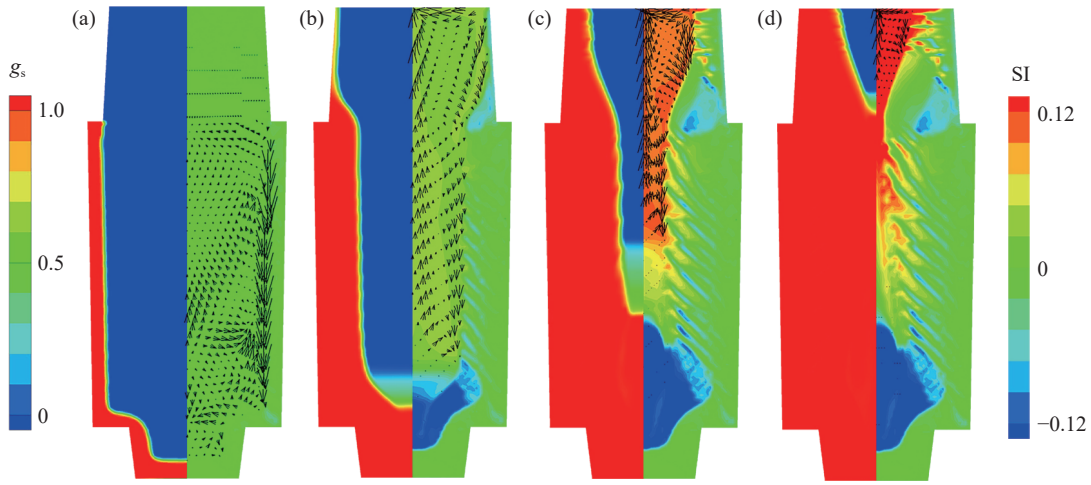

Fig. 3. Predicted solidification sequence of the 36-t ingot at different times: (a) 1000 s; (b) 6000 s; (c) 15000 s; (d) 25000 s. Left part: solid volume fraction $g_s = g_c + g_e$; right part: macrosegregation index (SI, contours) and liquid fluid flow (arrows).

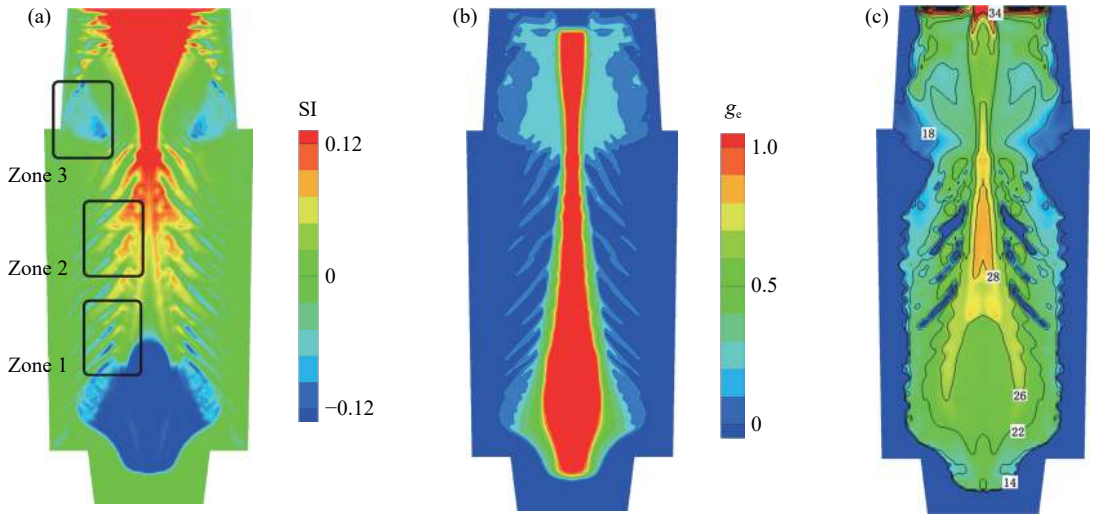

Fig. 4. Final result of the simulation: (a) concentration distribution; (b) solidification structure (volume fraction of equiaxed grains); (c) mean radius of equiaxed grains (in μm)..

grains, including both the free-floating and motionless grains. The structure adjacent to the chilling wall was dominantly columnar dendrite, and equiaxed grains occupied the inner space of the ingot. By comparing Figs. 4(a) and 4(b), it is found that the volume fraction profile of the equiaxed grains in the lower part coincided with the negative segregation cone. Moreover, the equiaxed grain distribution in the middle exhibited a similar morphology as the A-type segregations. As depicted in Fig. 4(b), the CET was observed where g_e sharply increased from 0.2 to 1. However, the reasons for CET was triggered in the lower and upper regions are different. In the lower part, the growth of columnar dendrite was suppressed by the stacked equiaxed grains under the effect of hard block [16]. In the upper part, the columnar dendrite was surpassed by the equiaxed grains in growth owing to the lack of undercooling.

Fig. 4(c) shows the distribution of the mean radius of the equiaxed grains. From the bottom and along the centerline of the ingot, the radius of the grain increased in the upward direction. A similar regularity was observed in a 3.3-ton ingot by Combeau *et al*. [6]. In the present study, the grains in the lower part were smaller because a large number of nuclei were generated from the solid shell in the early period. The larger grain radius in the upper part resulted from a lower nucleation but more grain growth. Additionally, large grains can be observed in the channels shown in Fig. 4(a).

The simulation results of the 36-t steel ingot shown in Fig. 4(a) were compared with the experimental measurements, as similarly reported by Tu *et al.* [11], and a good quantitative agreement was obtained. In Fig. 5, the concentration value is extracted along the centerline and three horizontal lines at different heights of the ingot: 0.6, 1.8, and 2.8 m.

In Fig. 5(a), the negative segregation cone occupies approximately one-third the ingot height. The segregation index (SI) is approximately ~15% compared to ~10% from the measurement. This discrepancy could be attributed to two aspects. First, the morphology of the equiaxed grain was not modeled accurately; therefore, the drag force between the liquid and grain, which can affect the prediction of the final macrostructure and macrosegregation, was defined incorrectly. Second, the solute transport across the liquid–grain interface under the driving force of concentration difference was ignored, resulting in an underestimation of equiaxed grain concentration.

The prediction indicates that the concentration in the middle of the centerline is close to the initial value, which is supported by the experiment result. The accurate simulation of this section is meaningful because the middle of the ingot is always used for industrial manufacturing.

A positive segregation with an index of over 40% is predicted in the upper part, and this value is less than that of the experimental measurement. The mismatch is regarded to have resulted from the overlook in solidification shrinkage. According to the research by Wu *et al.* [9], the formation of a solidification cavity on the top of the ingot creates a difference in the morphology of the top-located positive segregation. Furthermore, the shrinkage is an important issue that needs to be investigated in future research.

Figs. 5(b)–5(d) show the concentrations (both predicted and measured) along three horizontal lines. In Fig. 5(b), the predicted concentration is slightly lower, but the trend is identical with that of the measurement. The width of the negative segregation cone is ~0.5 m at this height (0.6 m), which was precisely predicted by this model. In Fig. 5(c), the irreg-

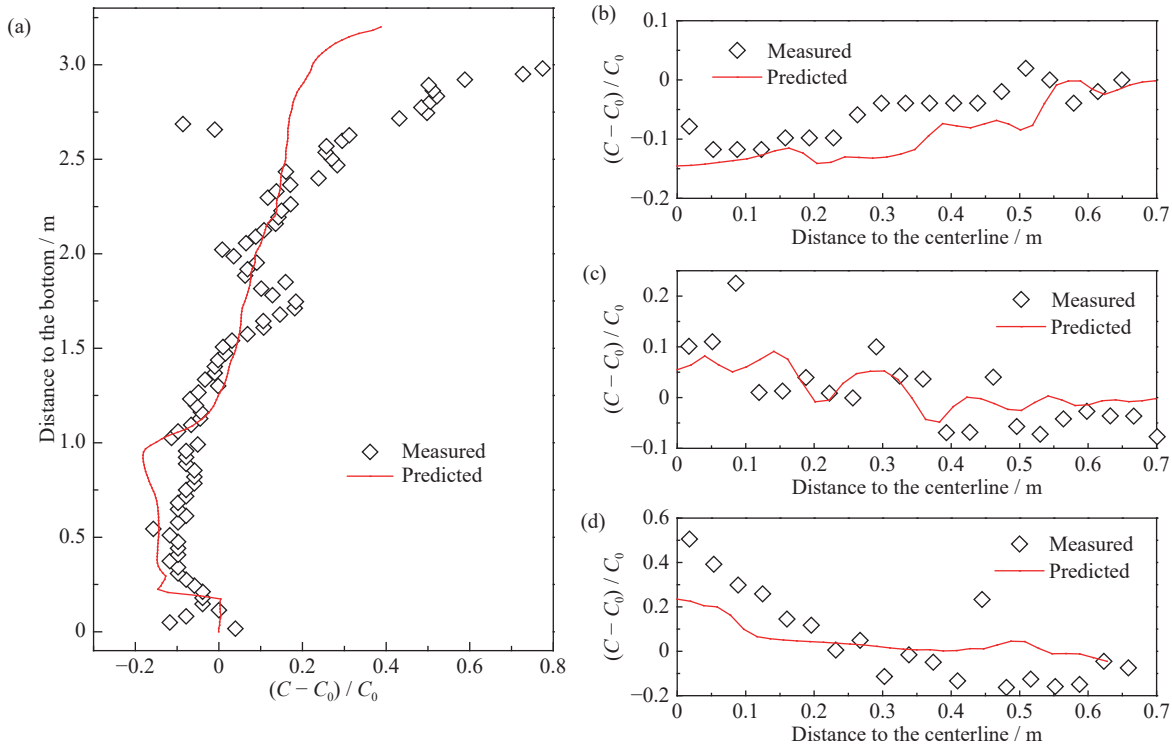

Fig. 5. Comparison of concentration between the numerical simulation and experimental measurements: (a) along the centerline of ingot; (b–d) along the horizontal line at the heights of 0.6, 1.8, and 2.8 m, respectively.

ular distribution of points indicates the presence of the A-type segregations. In Fig. 5(d), owing to the aforementioned reason, the prediction of positive segregation in the top is not as high as that of the measurement.

In summary, this model could reproduce the macrosegregation measured in the 36-t ingot. To further explore the characteristics of the macrosegregation, three zones of the ingot, as shown in Fig. 4(a), were chosen for an in-depth study.

4.2. Negative segregation at the ingot bottom

Fig. 6 illustrates the evolution of the negative segregation cone from 5000 s to 6000 s, corresponding to zone 1 in Fig. 4(a). Two clusters of settling equiaxed grains (with a radius greater or lower than a threshold) were extracted. Their corresponding flow fields are shown in the left and right parts of the subfigures. After nucleation, the equiaxed grains flowed in accordance with the liquid and spread all over the domain. In particular, only those adjacent to the solid front could coarsen because the undercooling condition was satisfied. On the contrary, the grains in the bulk melt were hindered from growing or even remelting owing to high temperature. As coarsening proceeded, the effect of excessive grain density over the liquid started to determine their settlement. Therefore, a flow of descending equiaxed grains was established along the solid front.

As shown in the left parts of Figs. 6(a) and 6(b), a broad

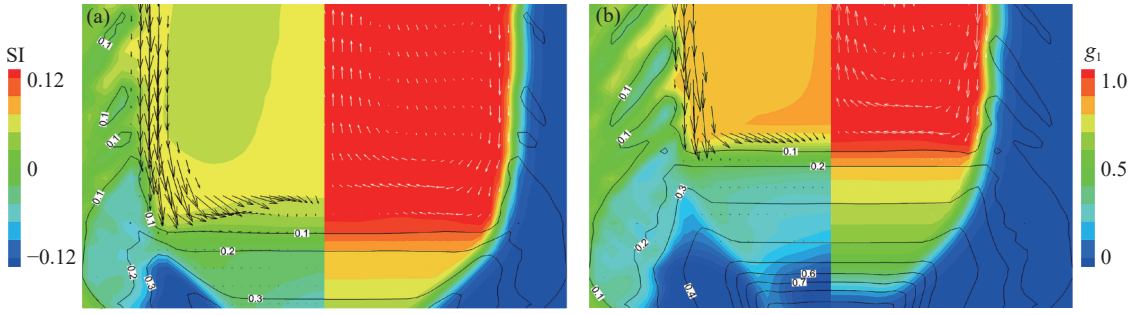

Fig. 6. Formation of negative segregation at the bottom: (a) 5000 s; (b) 6000 s. Left part of each subfigure: flow of large grains (black arrows) with solid fraction g_e (isoline) and segregation index SI (flood). Right part of each subfigure: flow of small grains (white arrows) with solid fraction g_e (isoline) and liquid fraction g_l (flood).

mushy zone was formed in the mid-bottom, including the stacked equiaxed grains and interdendritic melt. The velocities of both the phases reduced to nearly zero owing to the high viscosity of the equiaxed grains. During the coarsening of the equiaxed grains, the solute species was rejected by the dendrite and diffused into the liquid. With the increase in carbon concentration, the interdendritic melt was slowly forced into the bulk by the solutal buoyancy.

Two reasons contributed to the formation of the negative segregation in this area. The nuclei of the equiaxed grains originated from the solid front at a relatively high temperature; thus, the nuclei were lower in carbon concentration with reference to the phase diagram. Meanwhile, the solute-rich interdendritic melt in the mushy zone, as discussed above, rushed toward the bulk melt, thus inducing the loss of solute atoms from the zone.

4.3. A-type segregations in the ingot body

Fig. 7 illustrates the formation of A-type segregations at 11000 s (corresponding to zone 2 in Fig. 4(a)). The velocity of the liquid beyond a certain threshold was extracted and is indicated in the figure by arrows of the same length. Some pioneering theories [2] attribute such segregation to the behavior of the interdendritic flow in the mushy zone and solidification perturbation. In this study, the detailed process of channel formation is presented and the theories are supported.

Fig. 7(a) depicts the stable formation of several channels. The solute-enriched interdendritic melt squeezed through the mushy zone and joined the bulk melt. Fig. 7(b) shows the low solid volume fraction of such streak-like channels. This is because the interdendritic melt was lower in the liquidus and solidus owing to the solute enrichment. Thus, it tended to remelt the columnar dendrite on its way. The channels were 1 cm to 2 cm in width, with an inclined angle of 60°. The upward slope of the channels resulted from the dominance of the solutal buoyancy forces, because β_c was larger than β_t by four orders of magnitude. As observed in Fig. 4(c), the channels were later filled with large equiaxed grains. The high carbon concentration and low nucleation tendency account for this phenomenon.

The prediction of channel segregation using the current model was good. Nevertheless, more studies should be performed to relieve the segregation by modifying the casting technique.

4.4. Negative segregation near the riser neck

Negative segregation was found near the riser neck (zone 3 in Fig. 4(a)). Flemings [2] proposed a criterion G to estimate the occurrence of macrosegregation, where G is the scalar product of two vectors: temperature gradient and melt velocity. A negative value of G provides evidence of a negative segregation, while a positive value indicates a positive segregation. In particular, the absolute value of G represents the severity of segregation.

Figs. 8(a) and 8(b) show the predicted criterion G at 3000 and 10000 s, respectively, and Fig. 8(c) shows the final macrosegregation after solidification. In Fig. 8(a), the area by the front of the shell shows negative value of G at 3000 s, indicating the specific orientation relationship between temperature gradient and melt velocity. In Fig. 8(b) at 10000 s, such value of G by the front turns positive. The position of these two selected shell fronts corresponds respectively with the lower left and upper right edges of negative segregation as shown in Fig. 8(c), supporting evidence to the origin and termination of its formation. It can be inferred from this study that the negative segregation is affected by the configuration of the mold, especially the insulation ability of the hot top.

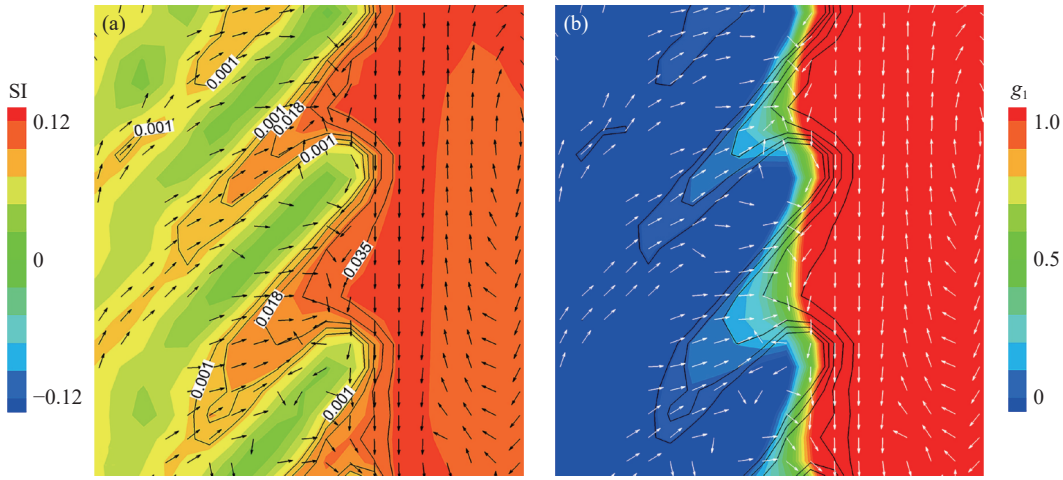

Fig. 7. Formation of A-type segregations at 11000 s: (a) segregation index SI (flood and isolines) with fluid flow (arrows); (b) segregation index SI (isoline) with liquid fraction g_l (flood) and fluid flow (arrows).

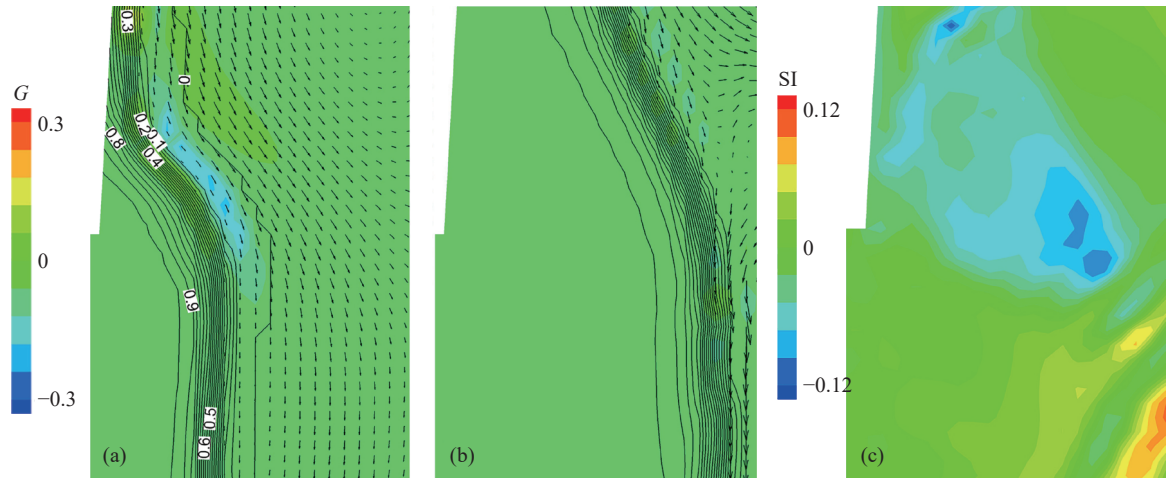

Fig. 8. Criterion of negative segregation (flood) and volume fraction of solid (lines) at 3000 s (a) and 10000 s (b); (c) final segregation index.

4.5. Criterion for the equiaxed grain settlement

Fig. 9 illustrates the quantitative comparison of simulation results along the centerline with three different criterion indexes, as mentioned in the model description. It should be noted that according to the model set, the trends of grain settlement increase from criterion I to III. In other words, the model with criterion I contains the most motionless equiaxed grains, and the model with criterion III contains the fewest. In the middle of the ingot, the simulation result with criterion II is very close to the measurements, which indicates the good rationality of this criterion index. By comparison, the predicted result with criterion I is lower than the measurements because the effect of grain settlement is underestimated. Similarly, the model with criterion III predicted a severer negative segregation by overestimating the grain settlement effect. In summary, the motionless equiaxed grains should also be considered for better simulation of the macrosegregation of large steel ingots, and more studies are needed in this aspect.

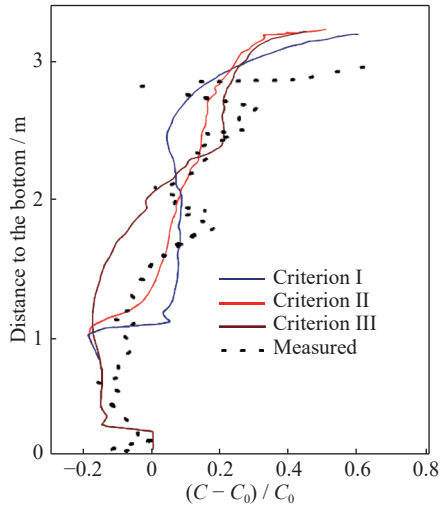

Fig. 9. Comparison of predicted segregation values along the centerline with different criteria.

5. Conclusions

A three-phase model to study phase motion and transformation was established for a macrosegregation simulation, and was verified using a 36-t steel ingot. A supplementary set of conservation equations were employed in the model to simulate the nucleation and growth of motionless equiaxed grains at the later stage of solidification. The typical segregation features–such as negative segregation at the bottom, positive segregation at the top, A-type segregations in the middle, and negative segregation close to the riser neck of the ingot were well-predicted by this model. The formation

of a negative segregation cone was investigated, and the importance of grain settlement was emphasized. The flow motion of the interdendritic melt in the mushy zone during the formation of A-type segregations was observed. An intense positive segregation was observed at the hot top because the remaining liquid contained a massive amount of solute species. The negative segregation close to the riser neck was observed as a result of the specific relationship between liquid flow and temperature gradient.

The predicted segregation pattern demonstrated a quantitative agreement with the experimental measurement. The quantitative discrepancy between the simulation and measurement was analyzed, and the reasons the discrepancy include (1) the incorrect modeling of phase interaction in a microscopic aspect and (2) the non-consideration of solidification shrinkage.

Acknowledgements

This work was financially supported by the project to strengthen industrial development at the grassroots level of the Ministry of Industry and Information Technology (MIIT), China (No. TC160A310/21). The cooperation of CITIC Heavy Industries Co., Ltd., Luoyang, China during the plant trials is gratefully acknowledged.

References

[1] E.J. Pickering, Macrosegregation in steel ingots: The applicability of modelling and characterization techniques, *ISIJ Int.*, 53(2013), No. 6, p. 935.

[2] M.C. Flemings, Our understanding of macrosegregation: Past and present, *ISIJ Int.*, 40(2000), No. 9, p. 833.

[3] C. Prakash, Two-phase model for binary solid–liquid phase change, Part I: governing equations, *Numer. Heat Transfer Part B*, 18(1990), p. 131.

[4] J. Ni and C. Beckermann, A volume–averaged two-phase model for transport phenomena during solidification, *Metall. Trans. B*, 22(1991), No. 3, p. 349.

[5] A. Ludwig and M.H. Wu, Modeling the columnar-to-equiaxed transition with a three-phase Eulerian approach, *Mater. Sci. Eng. A*, 413-414(2005), p. 109.

[6] H. Combeau, M. Založnik, S. Hans, and P.E. Richy, Prediction of macrosegregation in steel ingots: Influence of the motion and the morphology of equiaxed grains, *Metall. Mater. Trans. B*, 40(2009), No. 3, p. 289.

[7] M. Wu, A. Fjeld, and A. Ludwig, Modelling mixed columnar–equiaxed solidification with melt convection and grain sedimentation–Part I: Model description, *Comput. Mater. Sci.*, 50(2010), No. 1, p. 32.

[8] M. Wu, A. Fjeld, and A. Ludwig, Modelling mixed columnar—equiaxed solidification with melt convection and grain sedimentation—Part II: Illustrative modelling results and parameter studies, *Comput. Mater. Sci.*, 50(2010), No. 1, p. 43.

[9] M. Wu, A. Ludwig, and A. Kharicha, A four phase model for the macrosegregation and shrinkage cavity during solidification of steel ingot, *Appl. Math. Modell.*, 41(2017), p. 102.

[10] Z.H. Duan, W.T. Tu, B.Z. Shen, H.F. Shen, and B.C. Liu, Experimental measurements for numerical simulation of macrosegregation in a 36-ton steel ingot, *Metall. Mater. Trans. A*, 47(2016), No. 7, p. 3597.

[11] W.T. Tu, Z.H. Duan, B.Z. Shen, H.F. Shen, and B.C. Liu, Three-dimensional simulation of macrosegregation in a 36-ton steel ingot using a multicomponent multiphase model, *JOM*, 68(2016), No. 12, p. 3116.

[12] M.H. Wu, A. Ludwig, and A. Kharicha, Simulation of as-cast steel ingots, *Steel Res. Int.*, 89(2018), No. 1, p. art. No. 1700037.

[13] W.S. Li, H.F. Shen, and B.C. Liu, Numerical simulation of macrosegregation in steel ingots using a two-phase model, *Int. J. Miner. Metall. Mater.*, 19(2012), No. 9, p. 787.

[14] W.T. Tu, H.F. Shen, and B.C. Liu, Two-phase modeling of macrosegregation in a 231t steel ingot, *ISIJ Int.*, 54(2014), No. 2, p. 351.

[15] A. Ludwig and M.H. Wu, Modeling of globular equiaxed solidification with a two-phase approach, *Metall. Mater. Trans. A*, 33(2002), No. 12, p. 3673.

[16] J.D. Hunt, Steady state columnar and equiaxed growth of dendrites and eutectic, *Mater. Sci. Eng.*, 65(1984), No. 1, p. 75.